Computers & Geosciences 88 (2016) 9–21

Contents lists available at ScienceDirect

Computers & Geosciences

journal homepage: www.elsevier.com/locate/cageo

Case study

Estimating elastic moduli of rocks from thin sections: Digital rock study of 3D properties from 2D images

Nishank Saxena [a,b,*], Gary Mavko [b]

[a] Shell Technology Center Houston, Shell International Exploration & Production, Houston, Texas, USA
[b] Rock Physics Laboratory, Department of Geophysics, Stanford University, Stanford, California, USA

ARTICLE INFO

Article history:
Received 19 August 2015
Received in revised form
6 November 2015
Accepted 12 December 2015
Available online 17 December 2015

Keywords:
Digital rock
Image segmentation
Elastic moduli
Sandstone
Carbonate
Thin sections

ABSTRACT

Estimation of elastic rock moduli using 2D plane strain computations from thin sections has several numerical and analytical advantages over using 3D rock images, including faster computation, smaller memory requirements, and the availability of cheap thin sections. These advantages, however, must be weighed against the estimation accuracy of 3D rock properties from thin sections. We present a new method for predicting elastic properties of natural rocks using thin sections. Our method is based on a simple power-law transform that correlates computed 2D thin section moduli and the corresponding 3D rock moduli. The validity of this transform is established using a dataset comprised of FEM-computed elastic moduli of rock samples from various geologic formations, including Fontainebleau sandstone, Berea sandstone, Bituminous sand, and Grossmont carbonate. We note that using the power-law transform with a power-law coefficient between 0.4–0.6 contains 2D moduli to 3D moduli transformations for all rocks that are considered in this study. We also find that reliable estimates of P-wave (Vp) and S-wave velocity (Vs) trends can be obtained using 2D thin sections.

1. Introduction

Digital Rock Physics (DRP) is a fast evolving tool for rock property characterization that holds potential for reducing turnaround times for laboratory-based petrophysical analysis, as well as for geologic scenario testing. This tool is based on the idea that a representative rock image can yield important information on structural and volumetric properties (e.g., Fredrich et al., 1993; Golab et al., 2010; Arns et al., 2005; Andrä et al., 2013a), information that can be further used to simulate established physics at complex pore-grain boundaries to estimate elastic moduli (e.g., Arns et al., 2002; Dvorkin et al., 2011; Madonna, et al., 2012), electrical conductivity (e.g., Arns et al., 2001; Andrä et al., 2013b), and flow properties (e.g., Arns et al., 2004; Knackstedt et al., 2009; Dvorkin et al., 2011). In general, DRP computations are carried out using numerical techniques (e.g., finite element methods, Lattice–Boltzmann) on a three dimensional (3D) mesh generated from a high resolution image that is captured using modern imaging techniques (e.g., micro x-ray computer tomography, scanning electron microscopy).

DRP computations are impacted by challenges in imaging and segmentation, loss of resolution due to image reconstruction, and computer memory requirements. These challenges make DRP an expensive tool. In contrast, estimation of properties in two dimensions (2D) using rock thin sections is relatively easier and considerably cheaper. This allows for analysis of more grains in 2D than in 3D, given of course, that both 2D and 3D images have the same voxel size. Also, interpretation of thin sections is more familiar to petrologists, and thin sections are much more widely available than 3D images. These advantages of using 2D thin sections for analysis must be ultimately weighed against the ability to estimate accurate 3D properties using thin sections. Therefore, it is of considerable interest to address whether it is possible to utilize thin sections to gain some information on the corresponding property of the 3D media, especially in situations when 3D images are unavailable or are too expensive to acquire and process. Several authors have addressed this problem for estimating flow properties (e.g., Adler et al. 1990; Yeong and Torquato, 1998; Hilfer and Manwart, 2001; Øren and Bakke, 2002; Keehm, 2003).

However, no study to date has performed a detailed analysis of possible 2D–3D correlations between numerically computed elastic moduli of natural rocks. Therefore, the primary objective of this paper is to investigate the link between elastic moduli of natural rocks in 3D and the elastic moduli computed from its 2D slices (thin sections from the same 3D rock) under the plane strain boundary condition. We analyze a dataset that includes elastic moduli computed using the finite element method (FEM) for 12

* Corresponding author at: Shell Technology Center Houston, Shell International Exploration & Production, Houston, Texas, USA
E-mail addresses: nishank.saxena@gmail.com (N. Saxena), mavko@stanford.edu (G. Mavko).

http://dx.doi.org/10.1016/j.cageo.2015.12.008
0098-3004/

digital samples of natural rocks in 3D, along with the moduli of the corresponding 2D thin sections. For the rocks considered in this study, we note that a simple power-law relation can provide reasonably accurate estimates of rock moduli (in 3D) if only 2D information is available of the rock microstructure.

2. Digital rocks

We consider a total of twelve 3D digital rocks: four binary digital samples which were generated from segmented digital images of natural rocks–a Fontainebleau sandstone, a Berea sandstone, a Bituminous sand sample (referred as Bitumen Rock), and a Grossmont carbonate, and another eight digitally modified samples from the original four samples. This section describes these digital rocks:

2.1. Fontainebleau sandstone

The Fontainebleau sandstone sample image was taken from Andrä et al., (2013a). This image was previously obtained from ExxonMobil and was acquired using the synchrotron source at Brookhaven National Laboratory with a voxel scale of 7.5 μm. Fig. 1a shows the segmented binary digital rock ($288 \times 288 \times 300$) with grain and pore voxels. For this sample, the porosity is 14.7%, and permeability is around 1100 mD (Keehm, 2003). Fig. 2a shows the distribution of 2D thin section porosity as estimated from multiple slices of the original cube. Grains of Fontainebleau sandstone are typically composed of quartz (bulk modulus: 36 GPa; shear modulus: 45 GPa). In this paper, we refer to the original sample reported in Andrä et al. (2013a) as sample C. We generated two additional samples (A and B) by digitally expanding the grains of the original Fontainebleau sandstone sample C (shown in Fig. 4). Porosity of sample B is 11%, whereas the porosity of sample A is 5%.

2.2. Berea sandstone

The Berea sandstone dataset was also taken from Andrä et al., (2013a). Fig. 1b shows the segmented sample of size $800 \times 800 \times 800$ with a voxel edge length of 0.74 μm. Laboratory measured connected porosity of this sample is around 20%, and permeability was found to be between 200 and 500 mD. The reported porosity of the segmented digital sample is 18% (Andrä et al., 2013a). Fig. 2b shows the distribution of 2D thin section porosity. We refer to the original sample as sample C. Similar to the Fontainebleau samples, we also generated samples A and B by digitally expanding the grains of the original Berea sandstone sample C (shown in Fig. 3). Porosity of

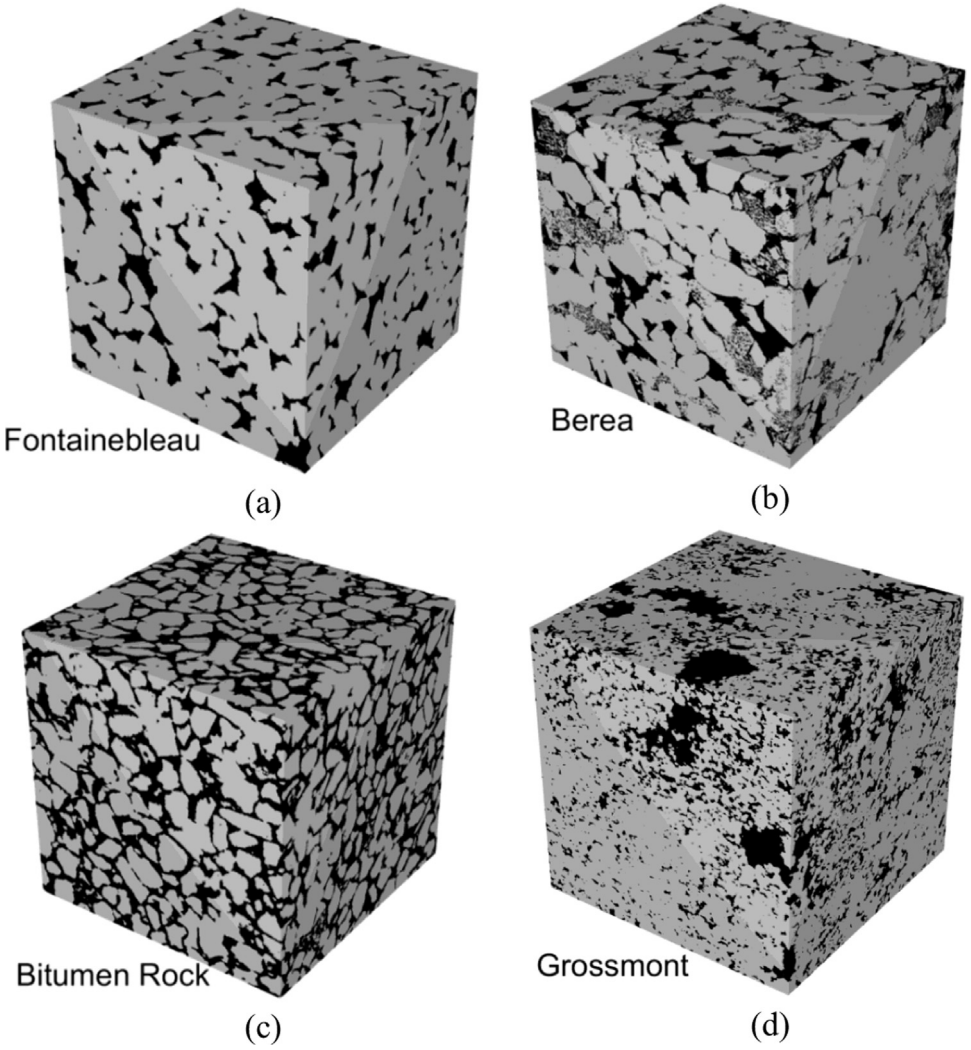

Fig. 1. Digital rocks: (a) Fontainebleau sandstone sample of size $288 \times 288 \times 300$, (b) Berea sandstone sample of size $800 \times 800 \times 800$, (c) Bitumen Rock sand sample of size $400 \times 400 \times 400$, (d) Grossmont carbonate sample of size $800 \times 800 \times 800$. Pores are shown in black and mineral in gray. Voxel edge length for Fontainebleau, Berea, Bitumen Rock, and Grossmont samples are 7.5 μm, 0.74 μm, 4 μm, and 2.02 μm, respectively.

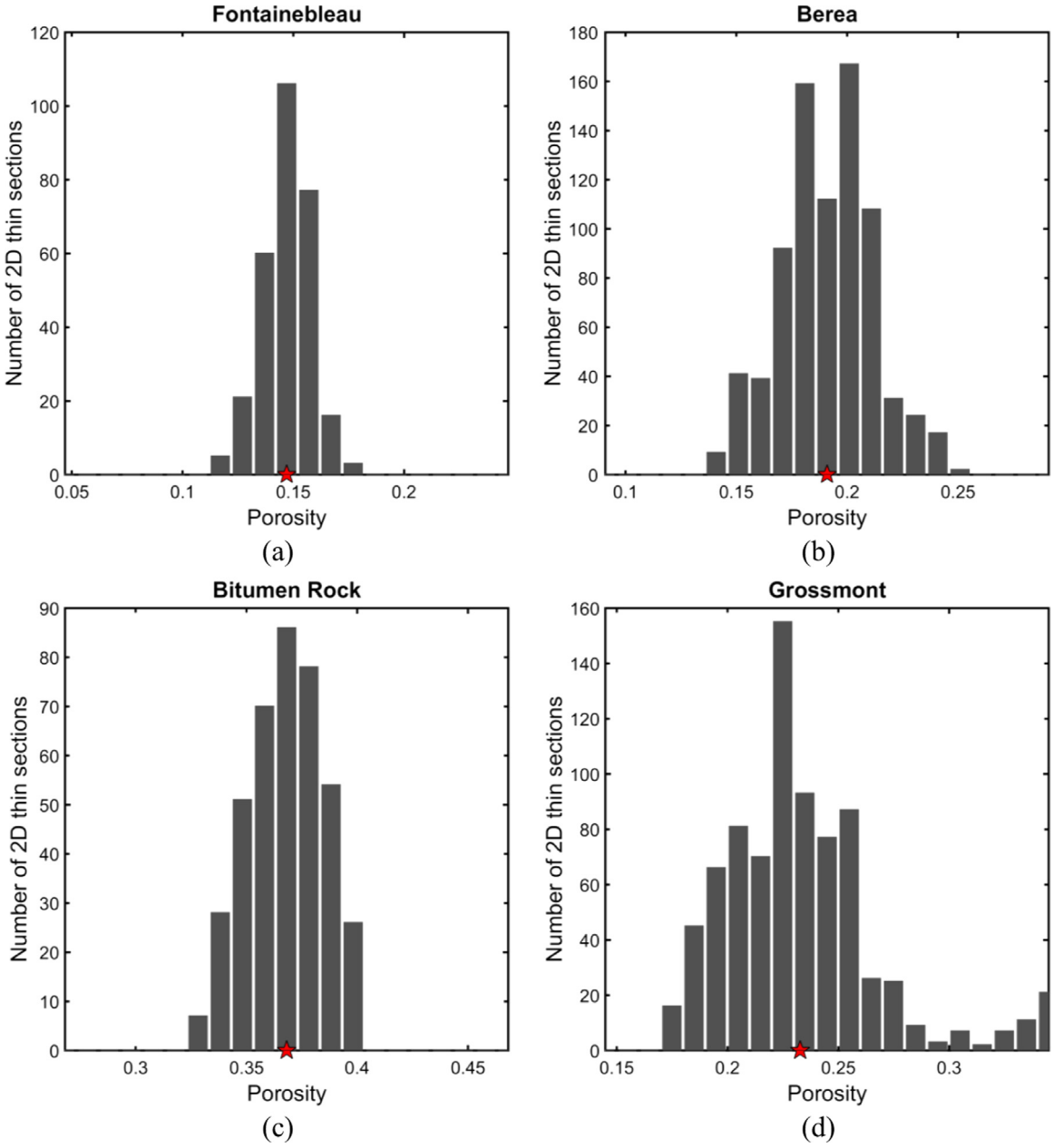

Fig. 2. Histograms of porosity estimated from thin sections for rock samples shown in Fig. 1. Average porosity from thin sections is shown with the red pentagon symbol.

sample B is 13%, whereas the porosity of sample A is 5%.

2.3. Bitumen rock

A digital bituminous sand rock sample was imaged, processed, and later segmented using commercially available Avizo software. The segmented digital sample of size $400 \times 400 \times 400$ is shown in Fig. 1c. The spatial resolution of this digital rock is 4 μm. Imaging revealed that the sample has quartz grains (volume fraction 0.56), bitumen-filled pores (volume fraction 0.37) and air-filled pores (volume fraction 0.07). To avoid partial saturation we digitally replaced all air-filled pores with quartz. This sample is referred to as Bitumen Rock sample C. Fig. 2c shows the distribution of 2D thin section porosity. Similar to our analysis of the Fontainebleau and Berea sandstone samples, we digitally alter the grains of Bitumen Rock sample C to generate samples B and A of porosity 17% and 5%, respectively (shown in Fig. 3).

2.4. Grossmont carbonate

The carbonate sample was also taken from Andrä et al., (2013a). The sample was extracted from the Grosmont formation, Alberta, Canada. Fig. 1d shows the digital rock sample of size $800 \times 800 \times 800$. The voxel edge length is 2.02 μm. The sample porosity is 24%, and laboratory measured permeability ranges from 150 mD to 470 mD. Fig. 2d shows the distribution of 2D thin section porosity. Altering grains of this original Grossmont carbonate sample C we generate samples B and A of porosity 13% and 5%, respectively (shown in Fig. 3).

3. Elasticity in 2D and 3D

For a 3D composite, Hooke's law of isotropic linear elasticity relates applied strains to the induced stresses by

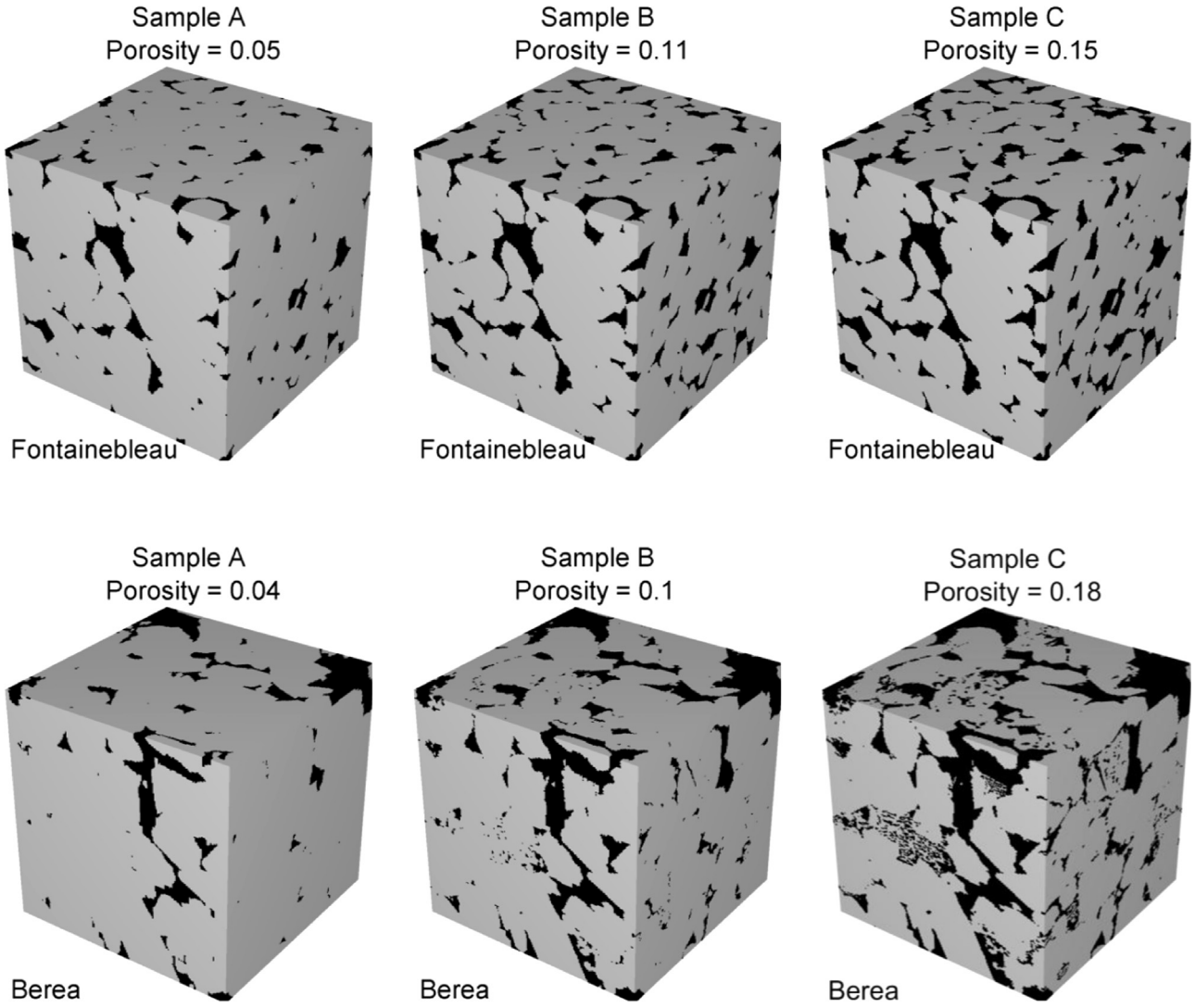

Fig. 3. Subcubes of the Fontainebleau and Berea sandstone samples that are shown in Fig. 1, original images are referred as "sample C". For each rock type, samples A and B are derived by expanding the grains in sample C resulting in reduced porosity. Each subcube is of size $200 \times 200 \times 200$. Pores are shown in black and mineral in gray. For these subcubes, the voxeledge length for the Fontainebleau and Berea samples are 7.5 μm and 1.48 μm, respectively.

$$\begin{bmatrix}\sigma_{11}\\ \sigma_{22}\\ \sigma_{33}\\ \sigma_{23}\\ \sigma_{13}\\ \sigma_{12}\end{bmatrix} = \begin{bmatrix} K_3+\frac{4}{3}G_3 & K_3-\frac{2}{3}G_3 & K_3-\frac{2}{3}G_3 & 0 & 0 & 0\\ K_3-\frac{2}{3}G_3 & K_3+\frac{4}{3}G_3 & K_3-\frac{2}{3}G_3 & 0 & 0 & 0\\ K_3-\frac{2}{3}G_3 & K_3-\frac{2}{3}G_3 & K_3+\frac{4}{3}G_3 & 0 & 0 & 0\\ 0 & 0 & 0 & G_3 & 0 & 0\\ 0 & 0 & 0 & 0 & G_3 & 0\\ 0 & 0 & 0 & 0 & 0 & G_3 \end{bmatrix} \begin{bmatrix}\varepsilon_{11}\\ \varepsilon_{22}\\ \varepsilon_{33}\\ 2\varepsilon_{23}\\ 2\varepsilon_{13}\\ 2\varepsilon_{12}\end{bmatrix}. \quad (1)$$

In Eq. 1, σ_{ij} are the volume averaged stresses and ε_{ij} are the volume averaged strains. Symbols K_3 and G_3 denote effective 3D bulk and shear moduli, respectively, which can be calculated using the following relations:

$$K_3 = \frac{1}{3}\frac{\sigma_{11}+\sigma_{22}+\sigma_{33}}{\varepsilon_{11}+\varepsilon_{22}+\varepsilon_{33}},\ G_3 = \frac{1}{2}\frac{\sigma_{12}}{\varepsilon_{12}}. \quad (2)$$

In this paper, we define a 2D composite as a 3D composite whose microstructural properties are fully described by a function that depends only on two dimensions (for example, directions 1 and 2) and does not vary in the third direction (direction 3). If direction 3 is perpendicular to the horizontal plane, the 2D medium will appear as a set of vertical pipes of arbitrary cross section parallel to direction 3. For such a composite, under the plane strain approximation ($\varepsilon_{23}=\varepsilon_{13}=\varepsilon_{32}=\varepsilon_{31}=\varepsilon_{33}=0$), the effective bulk and shear moduli can be defined as:

$$K_2 = \frac{1}{3}\frac{\sigma_{11}+\sigma_{22}+\sigma_{33}}{\varepsilon_{11}+\varepsilon_{22}},\ G_2 = \frac{1}{2}\frac{\sigma_{12}}{\varepsilon_{12}}. \quad (3)$$

Alternatively, the bulk modulus of a 2D composite, under plane strain, can also be defined as

$$K'_2 = \frac{1}{2}\frac{\sigma_{11}+\sigma_{22}}{\varepsilon_{11}+\varepsilon_{22}}. \quad (4)$$

For 2D composites the moduli K_2 and K'_2 are exactly related as

$$K'_2 = \frac{3}{2}\frac{K_2}{(1+\nu_{min})}. \quad (5)$$

The relation in Eq. 5 is valid for 2D composites with arbitrary shape empty holes, since under the plane strain boundary condition, σ_{33} is exactly related to $\sigma_{11}+\sigma_{22}$ as

$$\sigma_{33} = \nu_{min}(\sigma_{11}+\sigma_{22}), \quad (6)$$

where, ν_{min} is the 3D Poisson's ratio of the solid or mineral phase in the composite frame ($-1 \le \nu_{min} \le 0.5$). Further proof of relations in

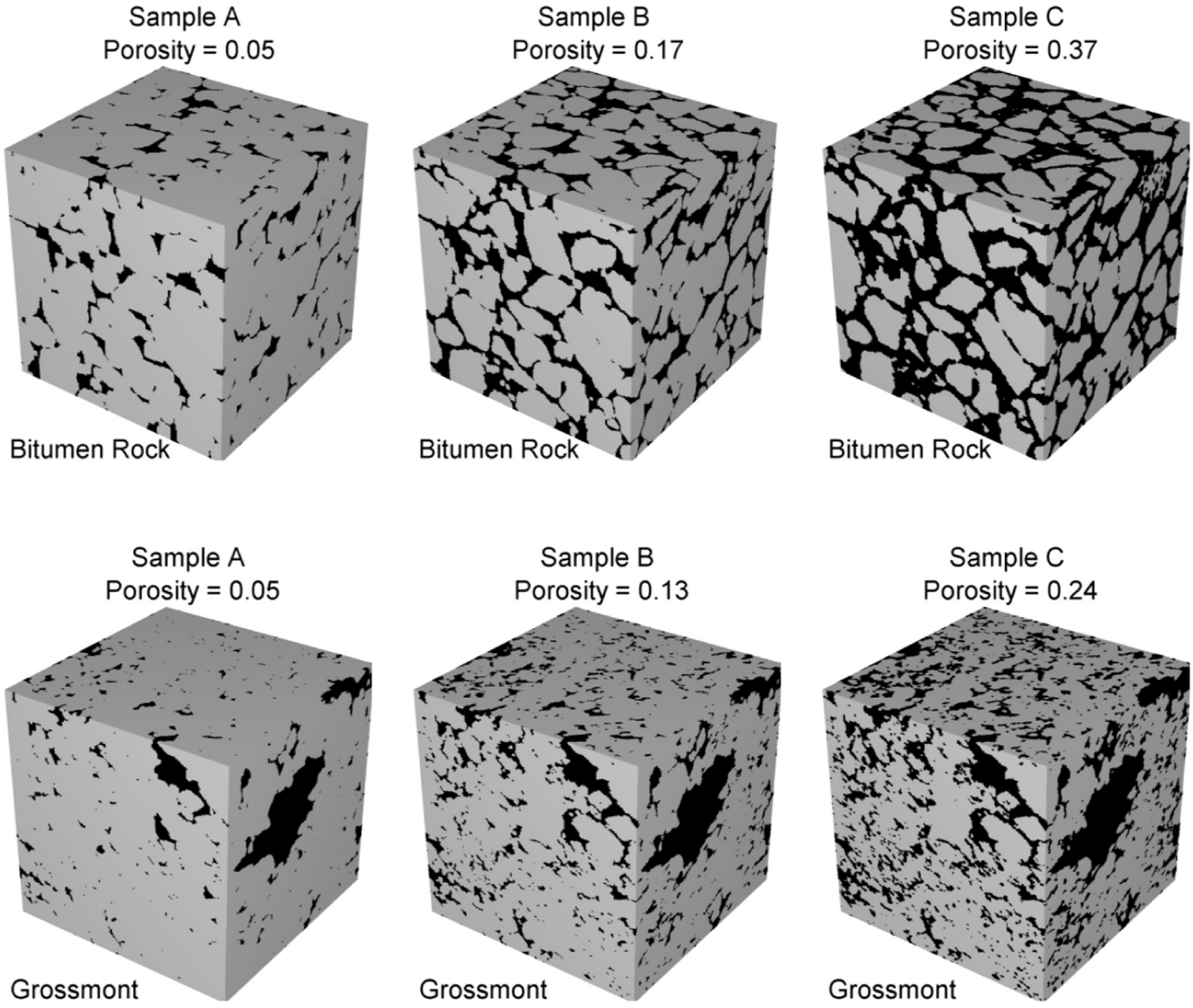

Fig. 4. Subcubes of Bitumen Rock and Grossmont carbonate samples that are shown in Fig. 1, original images are referred as "sample C". For each rock type, samples A and B are derived by expanding the grains in sample C resulting in reduced porosity. Each subcube is of size $200 \times 200 \times 200$. For these subcubes, the voxel edge length for the Bitumen rock and Grossmont samples are 4 μm and 4.04 μm, respectively.

Eqs. 5 and 6 is presented separately in Appendix A. For the remainder of the paper, we calculate the elastic moduli of 2D composites using the definition in Eq. 3, and we compare these moduli with the 3D moduli defined in Eq. 2. Throughout this paper, all non-porous phases (solid or liquid) have 3D elastic moduli, unless otherwise specified.

Hashin and Shtrikman, (1963) and Hashin, (1965) give bounds on elastic bulk and shear moduli for 3D composites (Torquato, 2002). The expressions for these bounds for an isotropic two-phase composite are given by

$$K^{HS+/-} = K^{(1)} + \frac{f_2}{\frac{1}{K^{(2)} - K^{(1)}} + f_1\left(K^{(1)} + \frac{4}{3}G^{(1)}\right)^{-1}}, \tag{7}$$

$$G^{HS+/-} = G^{(1)} + \frac{f_2}{\frac{1}{G^{(2)} - G^{(1)}} + f_1\left(G^{(1)} + \frac{G^{(1)}}{6}\left(\frac{9K^{(1)} + 8G^{(1)}}{K^{(1)} + 2G^{(1)}}\right)\right)^{-1}}, \tag{8}$$

where the superscripts (1) and (2) refer to the properties of the two phases. Eqs. 7 and 8 yield the upper bound when $K^{(1)}$ and $G^{(1)}$ are the *maximum* bulk and shear moduli of the individual phases, and the lower bounds when $K^{(1)}$ and $G^{(1)}$ are the *minimum* bulk and shear moduli of the phases. Superscripts $HS+$ and $HS-$ designate upper and lower bounds, respectively.

4. Computed moduli and results

To estimate elastic properties of digital rocks (3D composites) and thin Section (2D composites under the plane strain approximation) we use an implementation of the finite element method of Garboczi (Garboczi, 1998; Meille and Garboczi, 2001; Roberts and Garboczi, 2002). Andrä et al., (2013b) recently compared this FEM implementation with other numerical schemes. The following sample sizes were used in the property computations: 3D Fontainebleau sandstone sample of size $288 \times 288 \times 300$ and thin sections of size $288 \times 288 \times 1$, 3D Berea sandstone sample of size $800 \times 800 \times 800$ and thin sections of size $800 \times 800 \times 1$; 3D Bitumen Rock sand sample of size $400 \times 400 \times 400$ and thin section of size $400 \times 400 \times 1$; 3D Grossmont carbonate sample of size $800 \times 800 \times 800$ and thin section of size $800 \times 800 \times 1$. For 3D calculations the composites are subjected to the strain boundary conditions: $\varepsilon_{11} = \varepsilon_{22} = \varepsilon_{33} = 0.001$, $2\varepsilon_{23} = 0.001$, $2\varepsilon_{13} = 0.002$, and $2\varepsilon_{12} = 0.003$. Similarly, for 2D calculations the thin

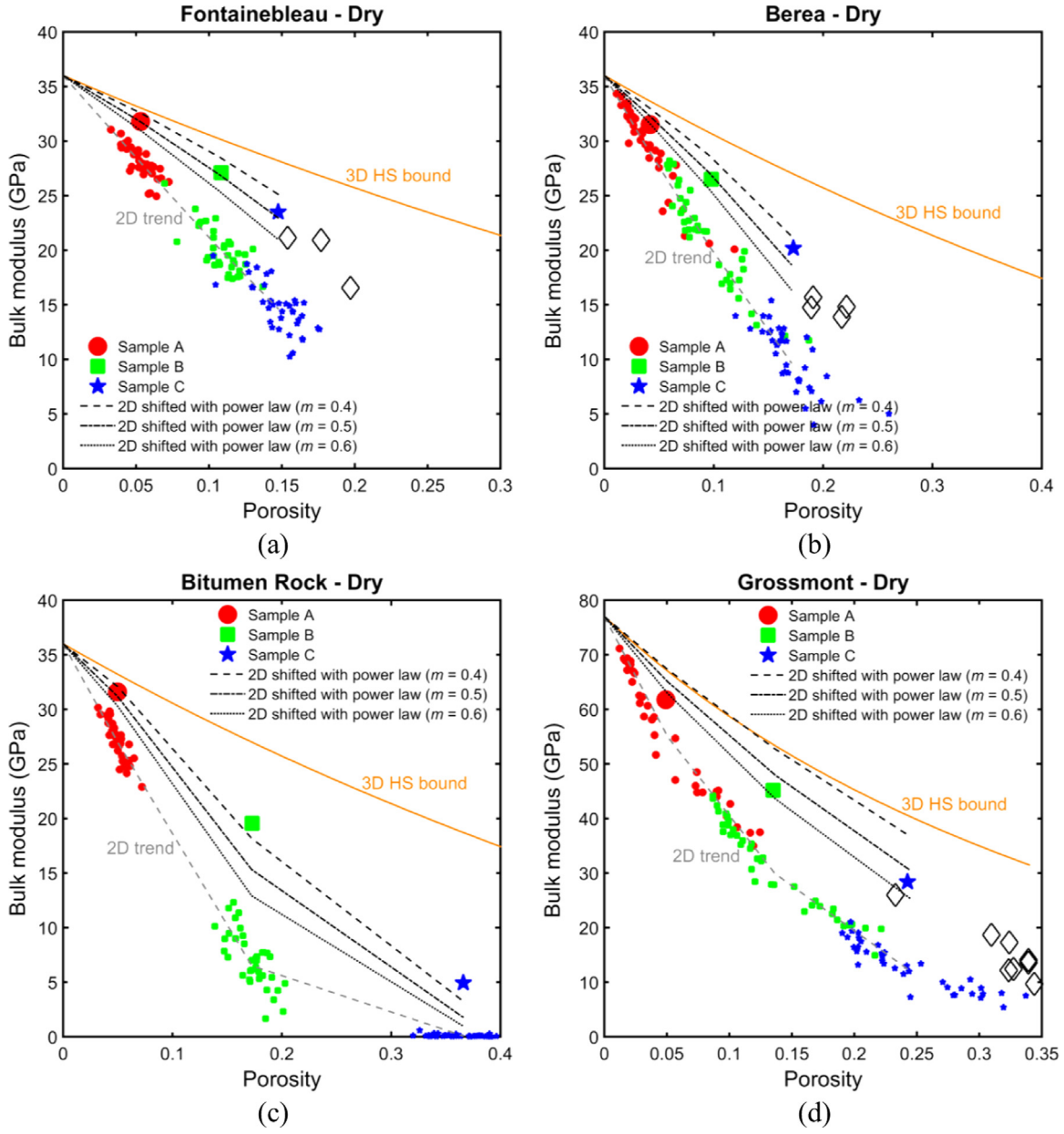

Fig. 5. Dry rock bulk modulus versus porosity for different rock samples. Calculations are shown for the 3D rock samples (large symbols) and the corresponding thin sections (40 for each rock sample; smaller symbols). Also shown are the Hashin–Shtrikman upper bounds on dry rock moduli versus porosity. The computed 2D moduli versus porosity trend is shown in dashed gray curve; this curve is modified using the power-law solution with different exponent values: 0.4, 0.5, and 0.6. Laboratory data points are taken from Han's, (1986) Fontainebleau and Berea dry measurements at 40 MPa, Carbonate taken from Vanorio et al., (2008).

sections are subjected to the plane strain boundary conditions with the non-zero strains: $\varepsilon_{11} = \varepsilon_{22} = 0.001$ and $2\varepsilon_{12} = 0.001$.

The computed effective bulk and shear moduli for the digital rocks and the corresponding thin sections (40 for each 3D sample) are shown in Figs. 5 and 6, respectively. Computed 3D moduli are as defined in Eq. 2 (large dots in the figures), and 2D moduli computed from the thin sections are as defined in Eq. 3 (small dots in the figures). Computations were performed with quartz as the mineral in the rock frame for Fontainebleau sandstone, Berea sandstone and Bitumen rock, and calcite as the mineral in the rock frame for Grossmont carbonate. These calculations were performed for composites with empty or dry pores. A summary of all parameters and numerical computation results is given in Tables 1–5. We also list the computed elastic properties when pores are saturated with water (bulk modulus 2.25 GPa and shear modulus 0 GPa) and a soft solid (bulk modulus 3 GPa and shear modulus 0.1 GPa). The computed properties of 3D digital rocks show trends consistent with those exhibited by laboratory measurements (shown in diamond symbols in Figs. 5 and 6), even though the laboratory measurements were neither taken on the same samples nor at the same scale as the digital computations.

Next, using the Voigt–Reuss–Hill averaging technique (i.e., $(\langle M\rangle + 1/\langle M^{-1}\rangle)/2$, such that M denotes individual moduli and the operator $\langle\rangle$ denotes arithmetic average) we calculate the average 2D bulk and shear moduli of all 40 thin sections drawn from the same 3D rock sample. To calculate the average 2D moduli we give equal weightage to each thin section regardless of the thin section porosity. The average thin section porosity is nearly identical to the 3D rock sample from which the thin sections were drawn. The calculated average dry-rock moduli–porosity trends are shown in Figs. 5 and 6. Interestingly, the computed 3D moduli–porosity and the calculated average 2D moduli–porosity trends can be approximately related by the simple empirical transforms:

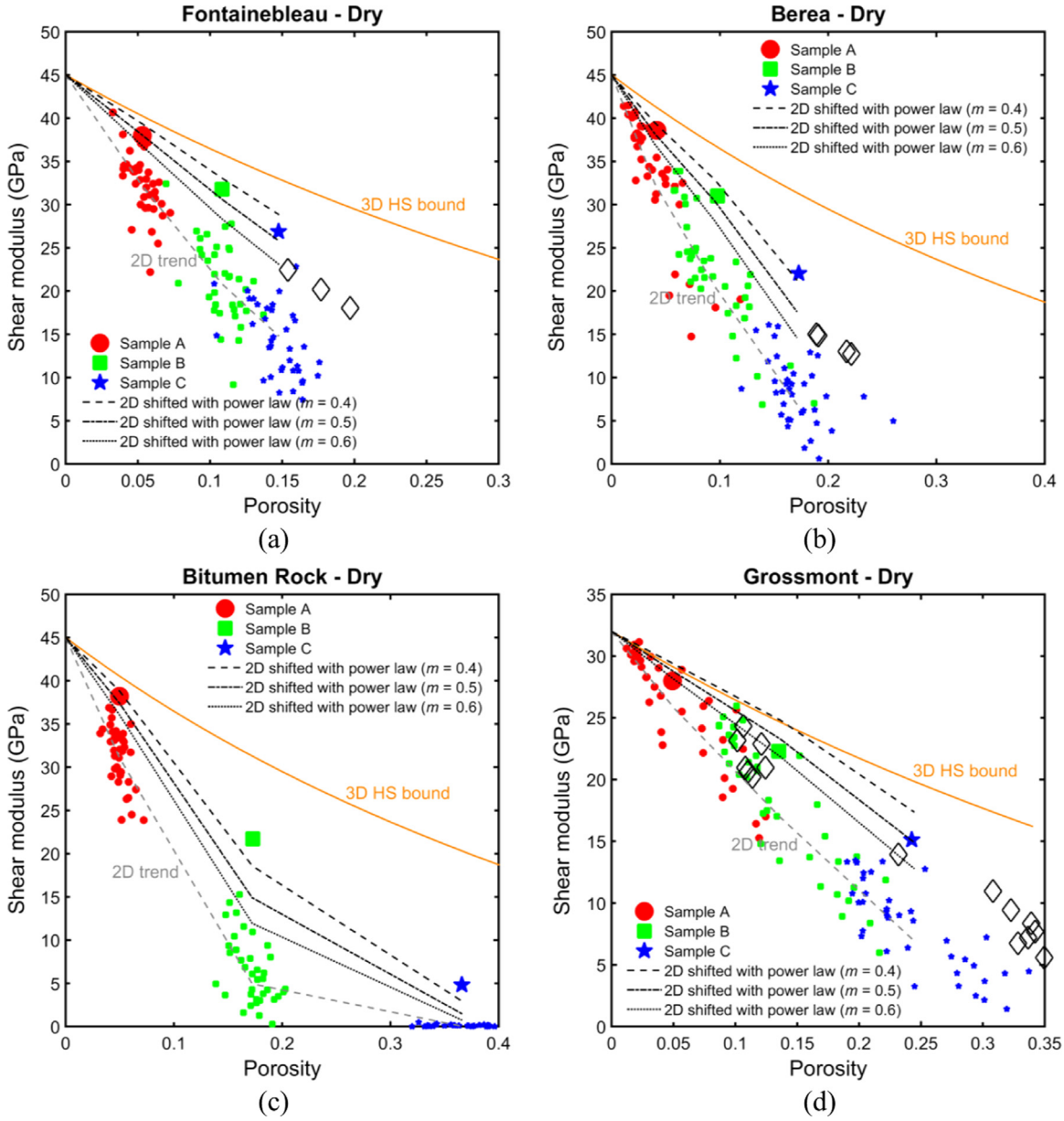

Fig. 6. Dry rock shear modulus versus porosity for different rock samples. Calculations are shown for the 3D rock samples and the corresponding thin sections (40 for each rock sample). Also shown are the Hashin–Shtrikman upper bounds on dry rock moduli versus porosity. The computed 2D moduli versus porosity trend is shown in dashed gray curve; this curve is modified using the power-law solution with different exponent values: 0.4, 0.5, and 0.6. Laboratory data points are taken from Han's, (1986) Fontainebleau and Berea dry measurements at 40 MPa, Carbonate taken from Vanorio et al., (2008).

Table 1
Properties of different phases used in numerical simulations.

Phase	Bulk modulus (GPa)	Shear modulus (GPa)	Density (g/cc)
Quartz	**36**	**45**	**2.65**
Calcite	**77**	**32**	**2.7**
Water	**2.25**	**10^{-3}**	**1**
Soft solid	**3**	**0.5**	**0.9**
Dry	**0**	**0**	**0**

$$\frac{K_{3-dry}}{K_{min}} = \left(\frac{K_{2-dry}}{K_{min}}\right)^{m_K}, \tag{9}$$

$$\frac{G_{3-dry}}{G_{min}} = \left(\frac{G_{2-dry}}{G_{min}}\right)^{m_G}. \tag{10}$$

In Eqs. 9 and 10, K_{min} and G_{min} are bulk and shear moduli of the mineral in the rock frame, respectively. Symbols K_{3-dry} and G_{3-dry} denote the effective dry bulk and shear moduli of a 3D digital rock, respectively, whereas K_{2-dry} and G_{2-dry} are the effective dry bulk and shear moduli of a 2D thin section of the 3D digital rock in question, respectively. Coefficients m_K and m_G are power-law exponents.

In Figs. 5 and 6, we show the power law transformed Voigt–Reuss–Hill curve for the computed thin section moduli (as per Eqs. 9 and 10) for a range of power law coefficients. We note that varying the coefficients m_K and m_G between 0.4 and 0.6 leads to predictions that contain the corresponding 3D digital rock moduli. Moreover, using $m_K \approx m_G \approx 0.5$ we note a good fit between the computed and the predicted 3D moduli (from 2D thin section moduli in Eqs. 9 and 10) for the Fontainebleau and Berea sandstone samples. Coefficients $m_K \approx m_G \approx 0.4$ fit the Bitumen rock samples. Similarly, $m_K \approx m_G \approx 0.6$ fit the computations for the

Table 2
Results of Fontainebleau sandstone computations.

Property/Rock	Font A	Font B	Font C
Sample size	**288 × 288 × 300**	**288 × 288 × 300**	**288 × 288 × 300**
Pixel size	**7.5 μm**	**7.5 μm**	**7.5 μm**
3D porosity	**0.05**	**0.1**	**0.15**
2D porosity	**0.05 ± 0.01**	**0.1 ± 0.01**	**0.15 ± 0.02**
3D bulk modulus (GPa)			
(Quartz mineral, dry pore)	**31.8**	**27.1**	**23.5**
(Water-filled pore)	**32.4**	**28.3**	**25.1**
(Solid-filled pore)	**32.7**	**28.9**	**26.0**
2D bulk modulus (GPa)			
(Quartz mineral, dry pore)	**27.9 ± 1.3**	**20.3 ± 2.2**	**14.95 ± 2.4**
(Water-filled pore)	**29.6 ± 1.0**	**23.5 ± 1.6**	**19.36 ± 1.7**
(Solid-filled pore)	**30.3 ± 0.9**	**25.0 ± 1.4**	**21.4 ± 1.5**
3D shear modulus (GPa)			
(Quartz mineral, dry pore)	**38**	**31.8**	**26.9**
(Water-filled pore)	**38.1**	**31.9**	**27.0**
(Solid-filled pore)	**38.4**	**32.6**	**28.1**
2D shear modulus (GPa)			
(Quartz mineral, dry pore)	**32.4 ± 3.6**	**21.9 ± 4.5**	**14.0 ± 4.5**
(Water-filled pore)	**32.8 ± 2.8**	**22.8 ± 3.6**	**15.9 ± 3.5**
(Solid-filled pore)	**34.1 ± 2.3**	**25.2 ± 3.0**	**19.2 ± 2.8**

Table 3
Results of Berea sandstone computations.

Property/Rock	Berea A	Berea B	Berea C
Sample size	**800 × 800 × 800**	**800 × 800 × 800**	**800 × 800 × 800**
Pixel size	**0.74 μm**	**0.74 μm**	**0.74 μm**
3D porosity	**0.04**	**0.1**	**0.18**
2D porosity	**0.04 ± 0.02**	**0.1 ± 0.03**	**0.19 ± 0.04**
3D bulk modulus (GPa)			
(Quartz mineral, dry pore)	**31.5**	**26.5**	**20.1**
(Water-filled pore)	**32.1**	**27.8**	**22.5**
(Solid-filled pore)	**32.4**	**28.5**	**23.8**
2D bulk modulus (GPa)			
(Quartz mineral, dry pore)	**29.2 ± 3.9**	**20.9 ± 4.4**	**10.2 ± 3.1**
(Water-filled pore)	**30.7 ± 3.0**	**24.3 ± 3.5**	**16.3 ± 2.1**
(Solid-filled pore)	**31.4 ± 2.6**	**25.7 ± 3.0**	**18.9 ± 1.9**
3D shear modulus (GPa)			
(Quartz mineral, dry pore)	**38.6**	**31**	**22.0**
(Water-filled pore)	**38.8**	**31.3**	**22.5**
(Solid-filled pore)	**39.1**	**32.3**	**24.1**
2D shear modulus (GPa)			
(Quartz mineral, dry pore)	**32.9 ± 7.2**	**22.6 ± 6.4**	**8.9 ± 4.0**
(Water-filled pore)	**33.8 ± 6.3**	**23.7 ± 5.9**	**11.6 ± 3.2**
(Solid-filled pore)	**35.2 ± 5.4**	**26.2 ± 5.2**	**15.8 ± 2.8**

Table 4
Results of Bitumen rock computations.

Property/Rock	Bit. Rock A	Bit. Rock B	Bit. Rock C
Sample size	**400 × 400 × 400**	**400 × 400 × 400**	**400 × 400 × 400**
Pixel size	**4.0 μm**	**4.0 μm**	**4.0 μm**
3D porosity	**0.05**	**0.17**	**0.37**
2D porosity	**0.05 ± 0.01**	**0.17 ± 0.02**	**0.37 ± 0.03**
3D bulk modulus (GPa)			
(Quartz mineral, dry pore)	**31.6**	**19.6**	**4.9**
(Water-filled pore)	**32.3**	**22.2**	**9.7**
(Solid-filled pore)	**32.6**	**22.5**	**12.2**
2D bulk modulus (GPa)			
(Quartz mineral, dry pore)	**27.0 ± 2.5**	**7.0 ± 2.8**	**0.4 ± 0.2**
(Water-filled pore)	**29.2 ± 1.7**	**14.5 ± 1.9**	**5.3 ± 0.5**
(Solid-filled pore)	**30.1 ± 1.4**	**17.6 ± 1.6**	**8.2 ± 0.8**
3D shear modulus (GPa)			
(Quartz mineral, dry pore)	**38.2**	**21.7**	**4.8**
(Water-filled pore)	**38.3**	**22.1**	**5.3**
(Solid-filled pore)	**38.6**	**23.7**	**8.6**
2D shear modulus (GPa)			
(Quartz mineral, dry pore)	**31.6 ± 3.3**	**6.7 ± 4.0**	**0.3 ± 0.3**
(Water-filled pore)	**32.3 ± 3.0**	**10.1 ± 2.8**	**0.2 ± 0.2**
(Solid-filled pore)	**33.8 ± 2.5**	**14.7 ± 2.3**	**4.0 ± 0.9**

Table 5
Results of Grossmont computations.

Property/Rock	Grossmont A	Grossmont B	Grossmont C
Sample size	**800 × 800 × 800**	**800 × 800 × 800**	**800 × 800 × 800**
Pixel size	**2.02 μm**	**2.02 μm**	**2.02 μm**
3D porosity	**0.05**	**0.13**	**0.24**
2D porosity	**0.05 ± 0.03**	**0.13 ± 0.04**	**0.24 ± 0.04**
3D bulk modulus (GPa)			
(Calcite mineral, dry pore)	**61.7**	**45.2**	**28.4**
(Water-filled pore)	**63.1**	**47.9**	**32.1**
(Solid-filled pore)	**63.9**	**49.3**	**34.2**
2D bulk modulus (GPa)			
(Calcite mineral, dry pore)	**56.6 ± 11.5**	**31.0 ± 7.9**	**13.6 ± 4.2**
(Water-filled pore)	**59.7 ± 10.1**	**37.6 ± 7.4**	**21.3 ± 4.5**
(Solid-filled pore)	**61.2 ± 9.3**	**40.9 ± 7.0**	**25.2 ± 4.5**
3D shear modulus (GPa)			
(Calcite mineral, dry pore)	**28.0**	**22.3**	**15.1**
(Water-filled pore)	**28.1**	**22.4**	**15.4**
(Solid-filled pore)	**28.3**	**23.0**	**16.3**
2D shear modulus (GPa)			
(Calcite mineral, dry pore)	**26.1 ± 4.6**	**18.6 ± 5.1**	**8.6 ± 3.2**
(Water-filled pore)	**26.1 ± 4.5**	**18.9 ± 4.8**	**10.0 ± 3.0**
(Solid-filled pore)	**26.9 ± 3.8**	**20.5 ± 4.0**	**12.5 ± 2.7**

Grossmont carbonate samples.

In Fig. 7, we compare the calculated P and S-wave velocities (Vp, Vs) estimated from effective bulk and shear moduli of water-saturated 3D digital rocks and the corresponding 2D thin sections. Also compared for sandstones are the empirical Vp–Vs curves obtained by Castagna et al., (1993), Han, (1986), and Vernik et al., 2002, for water-saturated sandstones. For Grossmont carbonate rock we compare the empirical Vp–Vs curves obtained by Castagna et al., (1993) for wet limestone. We note that all digital computations (2D and 3D) for the Fontainebleau, Berea and Bitumen Rock samples are consistent with the empirical trends for sandstones. Similarly, computations for the Grossmont carbonate samples are consistent with the Castagna et al. empirical trend for wet limestone. In fact no empirical transformation using Eqs. 9 and 10 is needed to reproduce the known empirical Vp–Vs trends. This suggests that it might be possible to use thin sections to obtain a Vp–Vs trend, for example, to predict missing Vs from Vp.

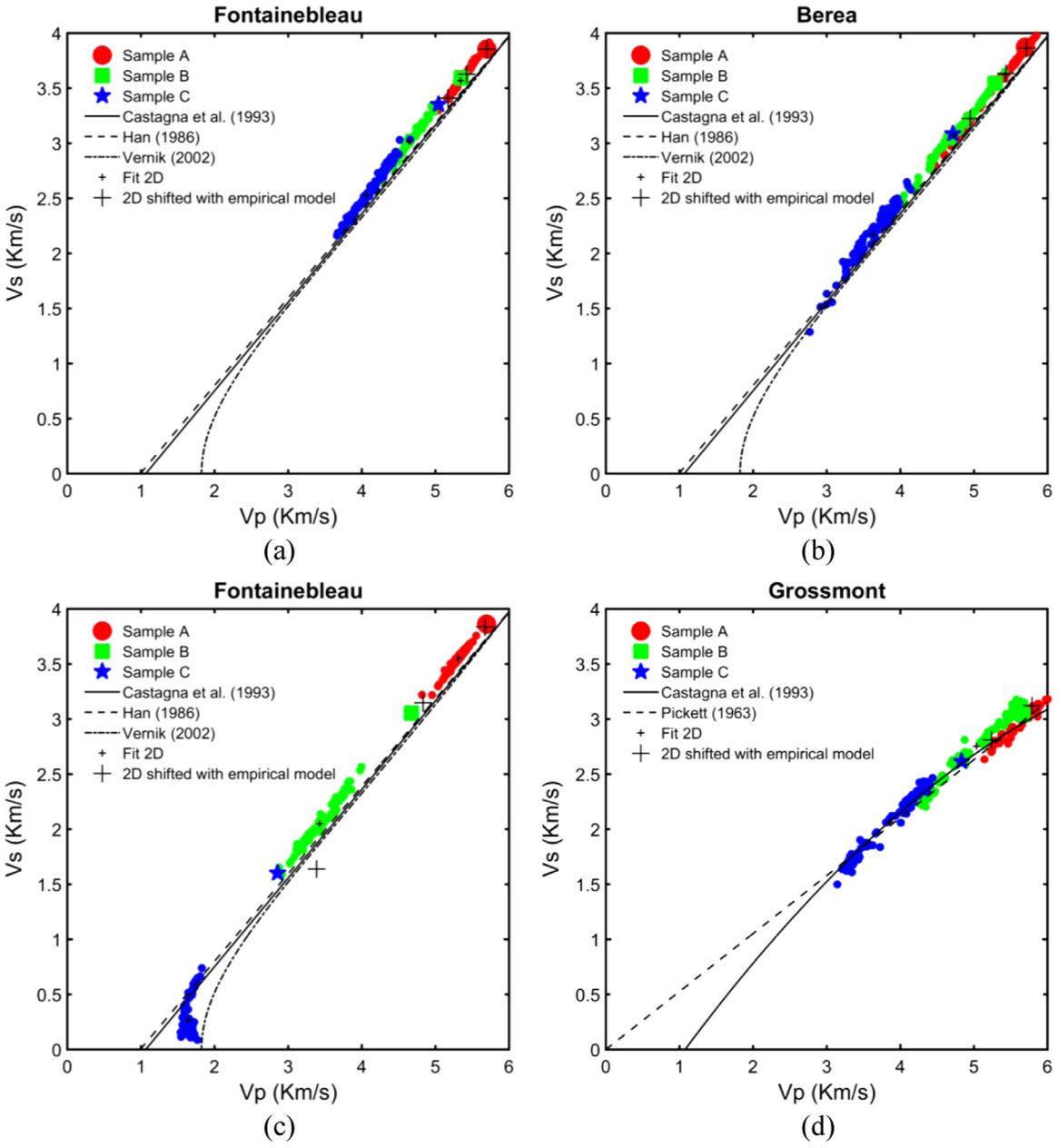

Fig. 7. Water-saturated (i.e., wet) rock Vp–Vs plots using computed elastic moduli from 3D rock samples and the corresponding 2D thin sections.

However, our numerical computations do not have sufficient variety in mineralogy to confirm this claim.

5. A simple empirical model

Many parameters can influence the power law exponents m_K and m_G, for example, pore shape, properties of the mineral and pore-fill material, porosity, Poisson's ratio of the mineral in the rock frame, etc. An exhaustive study on the impact of all possible parameters on power law exponents is beyond the scope of this paper. Instead we investigate the impact of rock porosity and Poisson's ratio of the mineral in the rock frame (ν_{min}) on the power law coefficients. To achieve this, we re-computed the moduli of all samples C digital rocks and the corresponding thin sections by digitally populating the mineral in the rock frame with K_{min} = 50 GPa and G_{min} varying between 0 and 75 GPa (That is, we use the actual imaged rock geometries, but apply a wide range of mineral moduli). This combination of K_{min} and G_{min} leads to variation in ν_{min} between 0.5 and 0. Fig. 8a and b show the computed power law coefficients for the average 2D moduli (i.e., Voigt–Reuss–Hill average of 40 thin section moduli for each 3D sample) as a function of ν_{min}. We note that the power law coefficients for all rocks generally increase with increase in the Poisson's ratio of the mineral in the rock frame. Similarly, in Fig. 9a and b we present numerical calculations of coefficients m_K and m_G for all twelve digital rocks (i.e., samples A, B, and C for each of the four rock types), such that the mineral in the rock frame for all rocks is quartz (these coefficients were calculated using the expressions in Eqs. 9 and 10 with average 2D moduli of 40 thin sections for each 3D sample). We note that the power law coefficients reduce with increase in porosity (φ). This finding is consistent with the

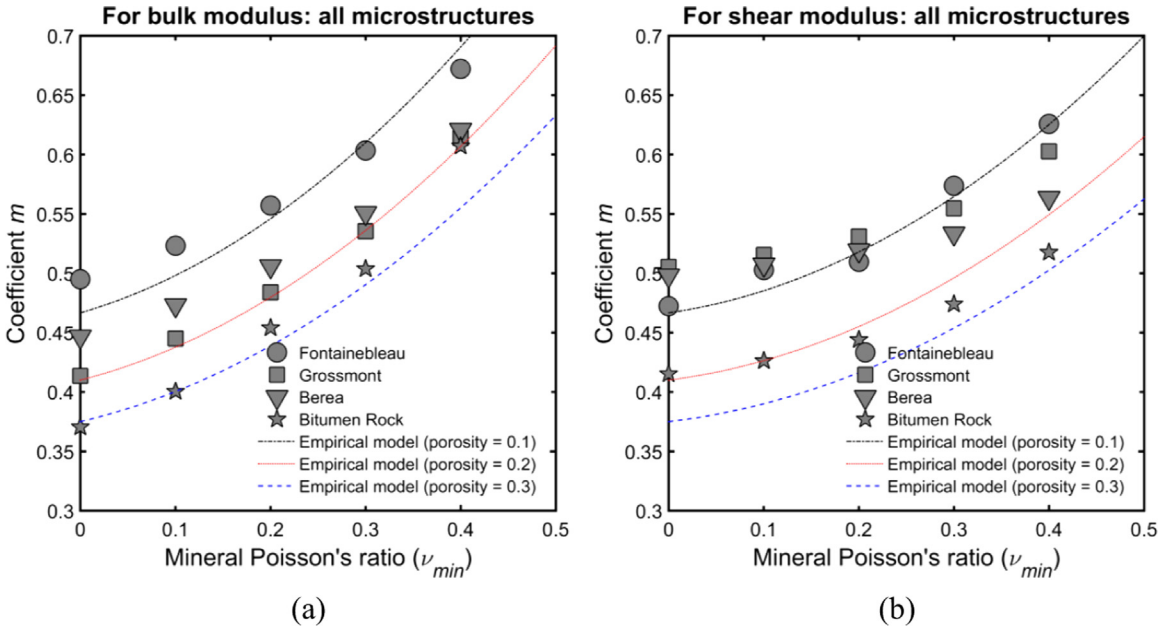

Fig. 8. Computed power-law exponent m for various rocks (as shown in the legend) versus rock mineral Poisson's ratio. Solutions of the empirical model are also shown for different porosities.

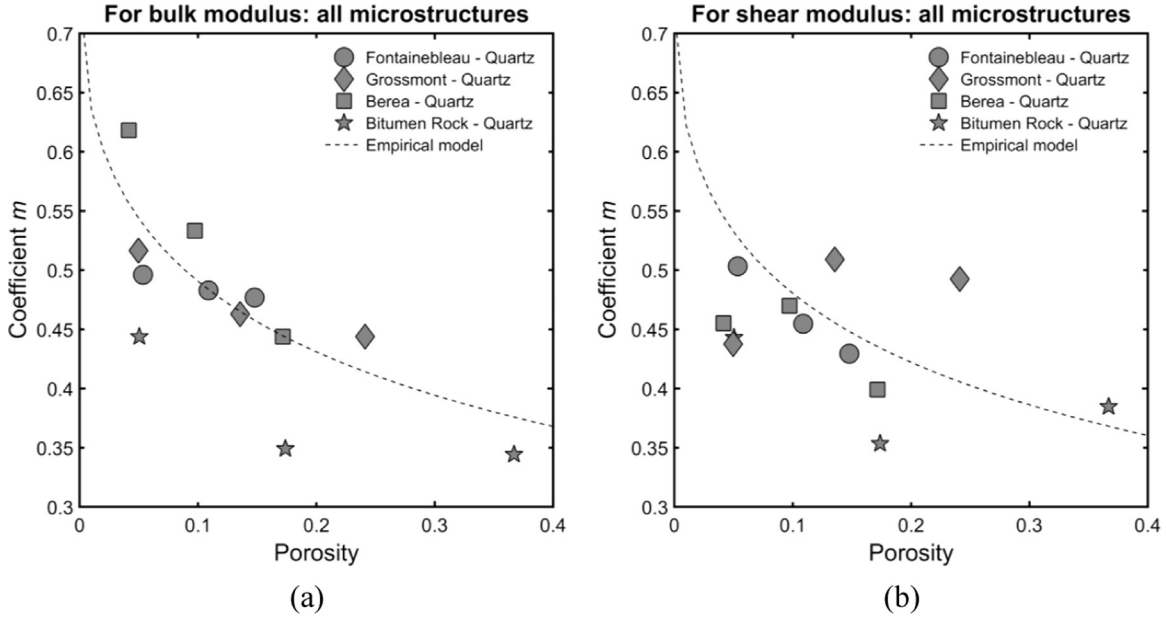

Fig. 9. Computed power-law exponent m for various rocks (as shown in the legend) versus porosity. The frame mineral in all rocks is quartz. Solution of the empirical model is also shown as a function of porosity.

observations of Meille and Garboczi, (2001) who showed that the critical porosity (φ_C, at which grain-to-grain contacts are lost) for a 2D thin section is generally lower than that of the corresponding 3D digital rock. Thus, as the thin section porosity approaches φ_C the power law coefficients should approach a relatively small value.

The data discussed in Figs. 8 and 9 can be fit by the following empirical model for the power law coefficients:

$$m_K = \frac{7}{4}\frac{\left(0.7\ \nu_{min}^2 + 0.2\ \nu_{min} + 0.4\right)}{1 + \sqrt{\varphi/\varphi_C}}, \tag{11}$$

$$m_G = \frac{7}{4}\frac{\left(0.6\ \nu_{min}^2 + 0.1\ \nu_{min} + 0.4\right)}{1 + \sqrt{\varphi/\varphi_C}}. \tag{12}$$

The empirical model coefficients in Eqs. 11 and 12 capture the observed reduction in power law coefficients with reduction in ν_{min} and an increase in porosity approaching the critical porosity value.

Figs. 10 and 11 show the predicted 3D digital rock moduli using the FEM-computed 2D thin section moduli with the empirical model (equations 9–12), for different rocks. For all rocks we assume $\varphi_C \approx 0.4$. For the Fontainebleau sandstone samples, the average disagreement between the predicted and computed 3D

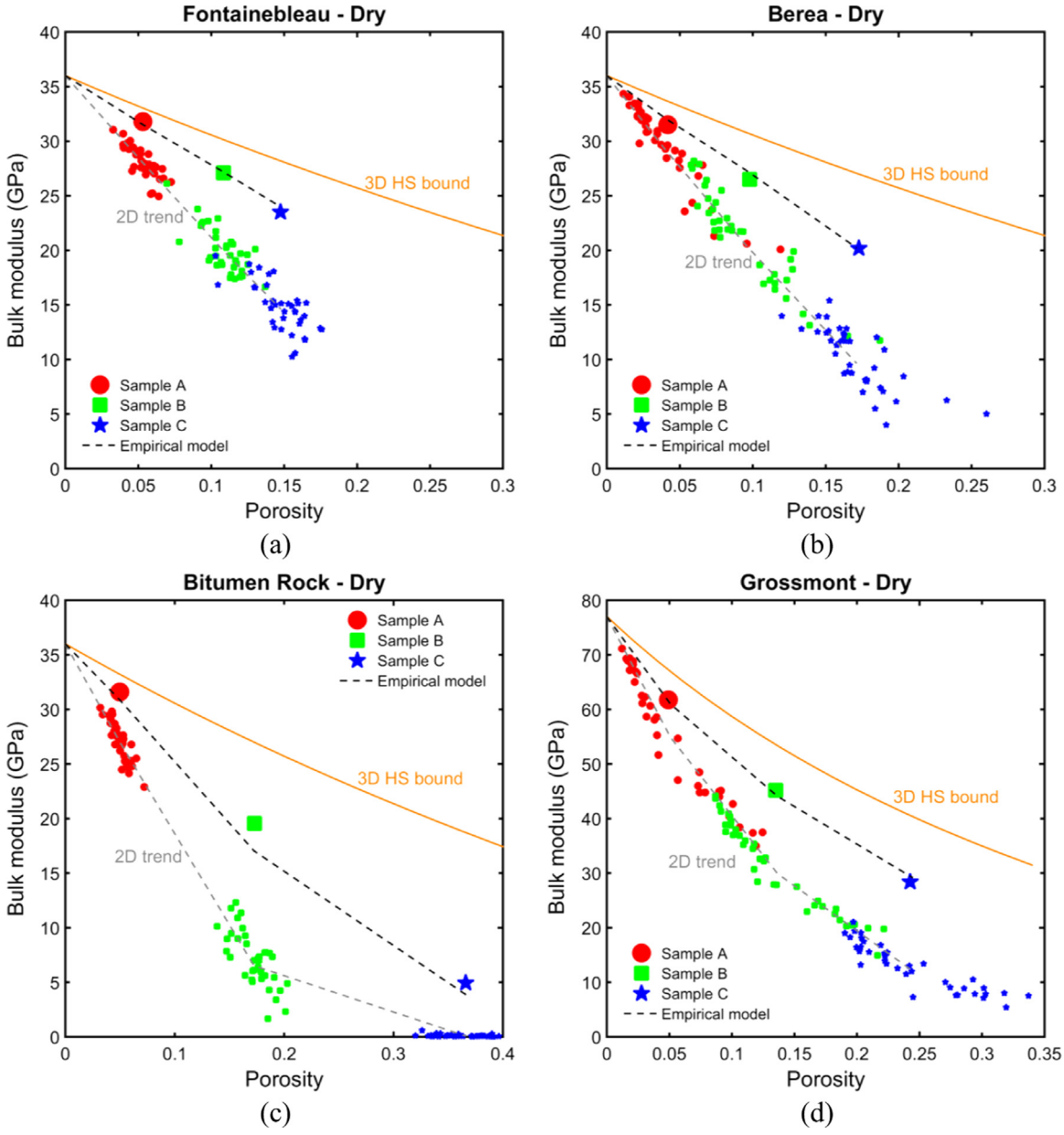

Fig. 10. Dry rock bulk modulus versus porosity for different rock samples. Calculations are shown for the 3D rock samples and the corresponding thin sections (40 for each rock sample). Also shown are the Hashin–Shtrikman bounds on dry rock moduli versus porosity. Predictions of 3D rock moduli using 2D moduli and the empirical model are shown in dashed black curves.

moduli (using the average 2D moduli trend) is about 1%. This disagreement for Berea sandstone and Grossmont carbonate samples is about 2% and 4%, respectively. However, the disagreement between the predicted and computed 3D moduli for Bitumen rock is relatively larger, about 10%.

6. Conclusions

We conclude that fairly accurate estimates of the effective elastic moduli of natural rocks (in 3D) can be obtained from 2D thin sections. This assertion is based on the numerical dataset presented in this paper which includes elastic moduli estimates of 12 digital rocks and 480 thin sections. To the best of our knowledge this is the first study on this subject encompassing digital samples of natural rocks. We find that the computed moduli of the 2D thin sections under plane strain boundary conditions are much softer than the moduli of the isotropic 3D rock. For the samples studied, we find that computed bulk (shear) moduli of a thin section can exhibit standard deviation from the average trend of up to 2.4 GPa (4.5 GPa) for Fontainebleau sandstone samples, 3.9 GPa (7.2 GPa) for Berea sandstone samples, 2.5 GPa (4 GPa) for Bitumen Rock samples, and 11.5 GPa (5.1 GPa) for Grossmont carbonate samples. The obtained Vp–Vs trends using the thin section moduli are consistent with the known empirical Vp–Vs trends which were previously established using laboratory and well log data. This could imply that moduli estimates using rock thin sections can yield valuable information on the Vp–Vs trend for a given rock type, which could also be used to predict Vs. However, this still requires further investigation.

We find that a power-law relation exists between the moduli computed for 3D digital rock and the corresponding 2D thin sections. For the

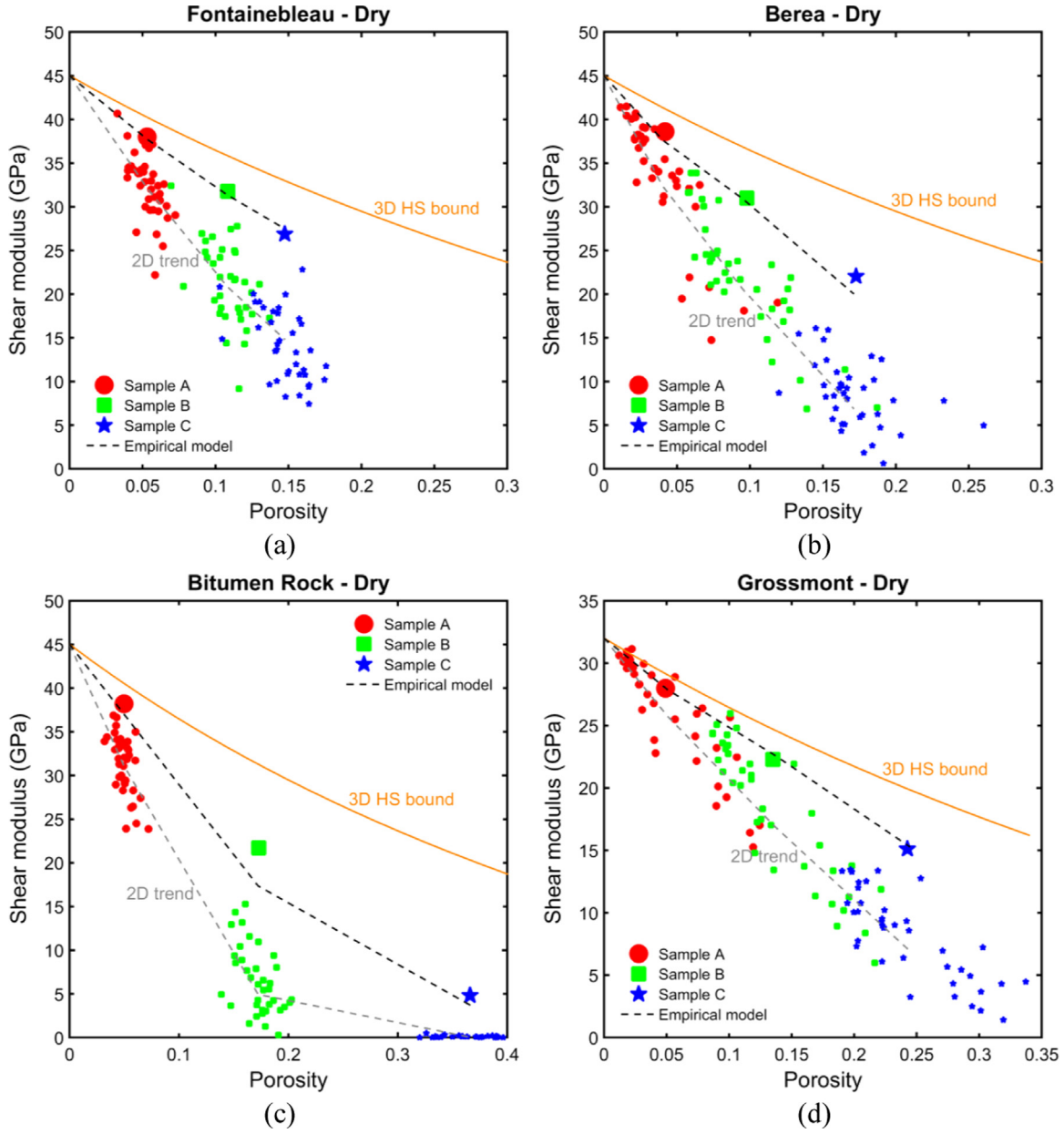

Fig. 11. Dry rock shear modulus versus porosity for different rock samples. Calculations are shown for the 3D rock samples and the corresponding thin sections (40 for each rock sample). Also shown are the Hashin–Shtrikman bounds on dry rock moduli versus porosity. Predictions of 3D rock moduli using 2D moduli and the empirical model are shown in dashed black curves.

rocks studied, the power-law coefficient was found to vary between 0.4 and 0.6. We find that the power-law coefficient depends on Poisson's ratio of the mineral in the rock frame and also on porosity. We propose an empirical model for predicting moduli of rocks when digital information on rock microstructure is available in 2D but not in 3D.

Acknowledgments

The authors would like to acknowledge Fabian Krzikalla for his initial work on the subject. Thanks to Jack Dvorkin and Amos Nur for discussions. Thanks to Jef Caers and four anonymous reviewers for their comments and suggestions that improved this paper.

Appendix A

Eqs. 5 and 6 can be obtained as follows. We consider a three-dimensional elastic object with empty pores. The solid (mineral) phase is homogeneous and linear elastic. The pore geometry is constant in the z-direction, so that the porous medium has VTI symmetry. Under plane strain loading with equal extensional strains in the x and y directions, Hooke's law can be expressed (Voigt notation) as

$$\begin{pmatrix}\sigma_{11}\\ \sigma_{22}\\ \sigma_{33}\end{pmatrix}=\begin{pmatrix}C_{11} & C_{12} & C_{13}\\ C_{12} & C_{11} & C_{13}\\ C_{13} & C_{13} & C_{33}\end{pmatrix}\begin{pmatrix}\varepsilon_0\\ \varepsilon_0\\ 0\end{pmatrix}. \tag{A-1}$$

In equation A-1, the stresses and strains are the volume

averages, and the constants $C_{ij}$are the effective elastic stiffnesses of the porous solid. From equation A-1 we obtain

$$(\sigma_{11} + \sigma_{22} + \sigma_{33}) = (C_{11} + C_{12} + C_{13})2\varepsilon_0, \tag{A-2}$$

The two moduli defined in Eqs. 3 and 4 are

$$K_2 \equiv \frac{(\sigma_{11} + \sigma_{22} + \sigma_{33})}{6\varepsilon_0}, \tag{A-3}$$

$$K'_2 \equiv \frac{(\sigma_{11} + \sigma_{22})}{4\varepsilon_0}. \tag{A-4}$$

Therefore

$$\frac{K_2}{K'_2} = \frac{2}{3}\left(1 + \frac{\sigma_{33}}{\sigma_{11} + \sigma_{22}}\right). \tag{A-5}$$

Under plane-strain loading of the z-independent geometry, the normal stresses at any point within the solid must satisfy

$$\sigma_{33}(x, y) = \nu_{min}\left[\sigma_{11}(x, y) + \sigma_{22}(x, y)\right], \tag{A-6}$$

where ν_{min} is the mineral phase Poisson's ratio. Taking the $(x–y)$ area average of equation A-6 over the solid phase at any z yields

$$\langle\sigma_{33}(x, y)\rangle_{min} = \nu_{min}\langle\sigma_{11}(x, y) + \sigma_{22}(x, y)\rangle_{min}. \tag{A-7}$$

It is also true that $\sigma_{33} = \langle\sigma_{33}\rangle_{min}(1 - \phi)$, and $(\sigma_{11} + \sigma_{22}) = \langle\sigma_{11} + \sigma_{22}\rangle_{min}(1 - \phi)$, so that equation A-7 yields the relation among the volume-averaged stresses and the mineral Poisson's ratio.

$$\sigma_{33} = \nu_{min}(\sigma_{11} + \sigma_{22}). \tag{A-8}$$

Inserting equation A-8 into equation A-5 gives

$$\frac{K_2}{K'_2} = \frac{2}{3}(1 + \nu_{min}). \tag{A-9}$$

References

Adler, P.M., Jacquin, C.G., Quiblier, J.A., 1990. Flow in simulated porous media. Int. J. Multiph. Flow. 16, 691–712.

Andrä, H., Combaret, N., Dvorkin, J., Glatt, E., Han, J., Kabel, M., Keehm, Y., Krzikalla, F., Lee, M., Madonna, C., Marsh, M., Mukerji, T., Saenger, E.H., Sain, R., Saxena, N., Ricker, S., Wiegmann, A., Zhan, X., 2013a. Digital rock physics benchmarks—Part I: imaging and segmentation. Comp. Geosci. 50, 25–32.

Andrä, H., Combaret, N., Dvorkin, J., Glatt, E., Han, J., Kabel, M., Keehm, Y., Krzikalla, F., Lee, M., Madonna, C., Marsh, M., Mukerji, T., Saenger, E.H., Sain, R., Saxena, N., Ricker, S., Wiegmann, A., Zhan, X., 2013b. Digital rock physics benchmarks—Part II: computing effective properties. Comp. Geosci. 50, 33–43.

Arns, C.H., Knackstedt, M.A., Pinczewski, W.V., Lindquist, W.B., 2001. Accurate computation of transport properties from microtomographic images. Geophys. Res. Lett. 28, 3361–3364.

Arns, C.H., Knackstedt, M.A., Pinczewski, W.V., Garboczi, E.G., 2002. Computation of linear elastic properties from microtomographic images: methodology and agreement between theory and experiment. Geophysics 67, 1396–1405.

Arns, C.H., Knackstedt, M.A., Pinczewski, W.V., Martys, N.S., 2004. Virtual permeametry on microtomographic images. J. Petr. Sci. Eng. 45, 41–46.

Arns, C.H., Bauget, F., Limaye, A., Sakellariou, A., Senden, T.J., Sheppard, A.P., Sok, R. M., Pinczewski, W.V., Bakke, S., Berge, L.I., Oren, P.E., Knackstedt, M.A., 2005. Porescale characterization of carbonates using X-Ray microtomography. Soc. Pet. Eng. J. 10, 475–484.

Castagna, J.P., Batzle, M.L., Kan, T.K., 1993. Rock physics: The link between rock properties and AVO response. In: Castagna, J.P., Backus, M.M. (Eds.), Offset-dependent reflectivity – Theory and practice of AVO analysis (Investigations in Geophysics): SEG vol. 8; 1993, pp. 135–171.

Dvorkin, J., Derzhi, N., Diaz, E., Fang, Q., 2011. Relevance of computational rock physics. Geophysics 76, E141–E153.

Fredrich, J., Greaves, K., Martin, J., 1993. Pore geometry and transport properties of Fontainebleau sandstone. Int. J. Rock. Mech. Miner. Sci. 30, 691–697.

Garboczi, E.J., 1998. Finite element and finite difference programs for computing the linear electric and elastic properties of digital image of random materials. Natl. Inst. Stand. Technol. Interag. Rep., 6269.

Golab, A., Knackstedt, M.A., Averdunk, H., Senden, T., Butcher, A.R., Jaime, P., 2010. 3D porosity and mineralogy characterization in tight gas sandstones. Lead. Edge 29 (12), 936–942.

Han, D., 1986. Effects of porosity and clay content on acoustic properties of sandstones and unconsolidated sediments. Stanford University, Stanford, California, United States, Ph.D. dissertation.

Hashin, Z., Shtrikman, S., 1963. A variational approach to the elastic behavior of multiphase materials. J. Mech. Phys. Solids 11, 127–140.

Hashin, Z., 1965. On elastic behaviour of fibre reinforced materials of arbitrary transverse phase geometry. J. Mech. Phys. Solids 13 (3), 119–134.

Hilfer, R., Manwart, C., 2001. Permeability and conductivity for reconstructed models of porous media. Phys. Rev. E 64, 021304.

Keehm, Y., 2003. Computational rock physics: Transport properties in porous media and applications. Stanford University, Stanford, California, United States, Ph.D. Dissertation.

Knackstedt, M., Latham, S., Madadi, M., Sheppard, A., Varslot, T., 2009. Digital rock physics: 3D imaging of core material and correlations to acoustic and flow properties. Lead. Edge 28, 28–33.

Madonna, C., Almqvist, B.S.G., Saenger, E.H., 2012. Digital rock Physics: Numerical prediction of pressure-dependent ultrasonic velocities using micro-CT imaging. Geophys. J. Int. 189 (3), 1475–1482.

Meille, S., Garboczi, E.J., 2001. Linear elastic properties of 2D and 3D models of porous materials made from elongated objects. Model. Simul. Mater. Sci. Eng. 9, 371–390.

Øren, P.E., Bakke, S., 2002. Process based reconstruction of sandstones and prediction of transport properties. Transp. Porous Media 46, 311–343.

Roberts, A.P., Garboczi, E.J., 2002. Elastic properties of model random three-dimensional open-cell solids. J. Mech. Phys. Solids 50, 33–55.

Torquato, S., 2002. Random Heterogeneous Materials: Microstructure and Macroscopic Properties. Springer-Verlag, New-York.

Vanorio, T., Scottelaro, C., Mavko, G., 2008. The effects of chemical and physical processes on the acoustic properties of carbonate rocks. Lead. Edge 27, 1040–1048.

Vernik, L., Fisher, D., Bahret, S., 2002. Estimation of net-to-gross from P and S impedance in deepwater turbidites. Lead. Edge 21, 380–387.

Yeong, C.L.Y., Torquato, S., 1998. Reconstructing random media. II. Three-dimensional media from two-dimensional cuts. Phys. Rev. E 58, 224–238.